NeuroImage 320 (2025) 121466

Contents lists available at ScienceDirect

NeuroImage

journal homepage: www.elsevier.com/locate/ynimg

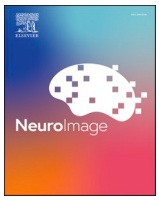

Exploring the contribution of gray matter microstructure to R1 contrast via multi-compartment diffusion modelling in the healthy brain

E. Bliakharskaia [a,b], A.M. Chiarelli [a,b,*], E. Patitucci [c], M. Carriero [a,b], D. Di Censo [a,b], E. Biondetti [a,b], C. Del Gratta [a,b], S. Capuani [d,e], M. Palombo [c,f], V. Tomassini [a,b,g,h], R.G. Wise [a,b], A. Caporale [a,b]

[a] Department of Neuroscience, Imaging and Clinical Sciences, 'G.D'Annunzio' University of Chieti-Pescara, Chieti, Italy
[b] Institute for Advanced Biomedical Technologies (ITAB), 'G.D'Annunzio' University of Chieti-Pescara, Chieti, Italy
[c] Cardiff University Brain Research Imaging Centre (CUBRIC), School of Psychology, Cardiff University, Cardiff, United Kingdom
[d] National Research Council - Institute for Complex Systems (CNR-ISC) c/o Department of Physics, Sapienza University of Rome, Piazzale Aldo Moro 5, 00185, Rome, Italy
[e] Santa Lucia Foundation, via Ardeatina 309, 00179 Roma, Italy
[f] School of Computer Science and Informatics, Cardiff University, Cardiff, United Kingdom
[g] MS Centre, Clinical Neurology, "SS. Annunziata" University Hospital, Chieti, Italy
[h] Centre for Disability, Rehabilitation and Sports Medicine (CARES), 'G.D'Annunzio' University of Chieti-Pescara, Chieti, Italy

ARTICLE INFO

Keywords:
DWI
SANDI
R1
Microstructure
Cortical myelination
Gray matter
White matter

ABSTRACT

The Soma And Neurite Density Imaging (SANDI) model enhances MRI-derived water diffusion metrics sensitivity to gray matter (GM) microstructural complexity. We investigated the hypothesis that the diffusion metrics derived from the SANDI three-compartment model contributed to the longitudinal relaxation rate R1(=1/T1) contrast in brain tissue. To this aim, twenty healthy volunteers underwent diffusion-weighted imaging and R1 mapping via MP2RAGE at 3 T. The diffusion metrics included intra-neurite signal fraction (fneurite), intra-soma signal fraction (fsoma), extra-neurite fraction (fextra), soma radii (Rsoma), and intra-neurite and extra-neurite diffusivities (D_{in} and D_e).

In GM, a moderate negative spatial correlation was observed between R1 and soma-related metrics (fsoma and Rsoma, with r = -0.47, -0.35, respectively), indicating that GM microstructure contributes to R1 contrast. These findings align with evidence suggesting structural heterogeneity in the cortex, where a different degree of cortical myelination modulates neuroplasticity. Notably, similar effects and trends were identified when evaluating across subjects' correlations of the metrics of interest (fsoma and Rsoma, with r = -0.56, -0.48, respectively). In WM, moderate to strong positive spatial correlations were observed between R1 and intra-neurite metrics (D_{in} and fneurite, with r = 0.53, 0.30, respectively), where myelinated axons host the pool of intra-neurite water.

These results suggest that WM and GM microstructural characteristics contribute to the R1 contrast, where R1 depends, among other factors, to the degree of myelination within brain tissues, thus contributing to the understanding of the emerging relaxation differences across the brain parenchyma. Future research should explore these relationships in clinical populations with demyelination and neurodegeneration.

1. Introduction

The myelin sheath, generating from the oligodendrocyte membranes wrapping around axons, plays a critical role in ensuring the efficient transmission of electrical signals between neurons. While it is traditionally associated with white matter (WM), significant amounts of myelin are found in the cortical gray matter (GM), where it may affect the organization and functional dynamics of intracortical circuits by stabilizing connections (Glasser et al., 2014). The mechanisms and functions of cortical myelination still need to be fully understood. Current hypotheses suggest that GM myelination plays a key role in neuroplasticity (Glasser et al., 2014), i.e. the brain's ability to adapt and

* Corresponding author at: Institute for Advanced Biomedical Technologies, Via Luigi Polacchi 66100, Chieti, Italy.
E-mail address: antonio.chiarelli@unich.it (A.M. Chiarelli).

https://doi.org/10.1016/j.neuroimage.2025.121466
Received 5 April 2025; Received in revised form 27 August 2025; Accepted 15 September 2025
Available online 16 September 2025

reorganize itself in response to learning, experience, or injury, and contributes to shaping neural pathways and supporting cognitive and motor functions. On the other hand, in diseases such as Multiple Sclerosis, cortical demyelination is associated with disease progression and worsening pathology (Kutzelnigg et al., 2005), and even at the earliest stages of the disease, aberrant GM myelination correlates with clinical impairment (Davies et al., 2004).

Myelin alters the magnetic properties of brain tissues by shortening T1, the MRI longitudinal relaxation time (T1), thus increasing R1 (=1/T1), the longitudinal relaxation rate. R1 is sensitive to the local microstructural properties such as the water-to-macromolecule ratio (i.e. effectively the water content) and the presence of iron (Callaghan et al., 2015; Gelman et al., 2001; Harkins et al., 2016; Desmond et al., 2016), in addition to being related to the myelin content. Indeed, a relationship of proportionality between R1 and brain myelin content has been demonstrated with higher myelin content resulting in larger R1 values (Mottershead et al., 2003; Schmierer et al., 2008, 2004). Additionally, there is strong evidence of correspondence between histological data and myelin patterns in the cortex observed via T1-weighted high-resolution MRI (Eickhoff et al., 2005), which can detect distinct myelination patterns across the cortex (Walters et al., 2003). As a result, R1 mapping has been widely adopted as a non-invasive technique to infer myelin content in vivo (Lutti et al., 2014).

In addition to influencing the tissue longitudinal relaxation rate because of its macromolecular structure, the presence of myelin in the voxel of tissue reduces the amount of free diffusion in that voxel, as axons are covered by a lipid protein bilayer, which hinders and restricts water diffusion. This latter mechanism is thought to originate from multiple diffusive compartments (Jones, 2010). Indeed, water diffusion varies within the brain parenchyma, exhibiting isotropic behaviour in GM and anisotropic properties in WM regions, characterized by densely packed myelinated fibres. By exploiting the endogenous contrast provided by self-diffusion of water molecules in tissues, diffusion-weighted MRI (DW-MRI) can be used to probe the microstructure of biological tissues permitting the study of brain development (Mukherjee et al., 2002) and the assessment of structural integrity in normal and pathological states (Caporale et al., 2017; Guerreri et al., 2019; Salat et al., 2005; Sullivan and Pfefferbaum, 2010).

The mathematical models that parameterize brain tissue microstructure from diffusion signals necessarily simplify the underlying cellular geometry, which may limit the accuracy and completeness of microstructure estimation (Alexander et al., 2019). Additionally, several key factors need to be considered for GM: water exchange across the cell membrane - between neurites and the extracellular space (Jelescu et al., 2022; Olesen et al., 2022); non-Gaussian diffusion along neuronal and glial processes - resulting from structural disorder (Novikov et al., 2014, 2011); the signal contribution from soma (Palombo et al., 2020). Traditional diffusion models have historically schematized neural tissue as a combination of two diffusive compartments: one corresponding to the confined space within the neurites (intra-neurite compartment), the other including the water diffusing in the extra-cellular space (extra-neurite compartment). However, recent studies have shown that the 'Standard Model' of diffusion (SM) with its two compartments fails in representing diffusion signal attenuation at high b-values (McKinnon et al., 2017; Palombo et al., 2018). As a result, diffusion MRI in GM requires 'rethinking the basic microstructure modeling blocks' to more accurately reflect the complex interplay between cellular compartments and diffusion processes (Jelescu et al., 2022). More recently, the intra-soma compartment (including neurons and neuroglia) was added in the Soma And Neurite Density Imaging (SANDI) diffusion model (Palombo et al., 2020). This model is particularly promising for studying cortical architecture and cortical myelination in that it describes water diffusion within tissue compartments more comprehensively.

Given these considerations, we hypothesized that GM microstructural characteristics, particularly its cytoarchitecture, contributing to R1 contrast, determined an association between SANDI-derived diffusion metrics in GM and R1. For completeness, we also investigated such associations in WM. Towards this aim, we decided to employ the Magnetization Prepared 2 Rapid Acquisition Gradient Echo (MP2RAGE) sequence (Marques et al., 2010) for R1 mapping as it is becoming increasingly widespread in research and it is a clinically viable approach, considering its contained acquisition time.

This study aims thus to determine whether specific microstructural properties captured by the SANDI model corresponded to variations in R1, which depends, among other things, on the myelin content.

By establishing these relationships, our study seeks to clarify the contribution of cytoarchitecture to R1 contrast, providing new insights into how neuronal architecture and myelin content interact in the healthy brain.

2. Methods

2.1. Theory – soma and neurite density imaging model

Traditional brain microstructure imaging models include two diffusive compartments, intra-neurite and extra-neurite, where neurites are modelled by infinite cylinders of null radius embedded in the hindered extra-neurite water. The extra-neurite pool in WM corresponds to water in the extra-axonal space, whereas, in GM, this pool includes both water in the extra-cellular space and water within the cell bodies of neurons and glia, called the soma, combined into a single diffusive compartment. This model is sufficient to describe DW-MRI signal attenuation in WM and GM for diffusion weights up to $b = 3000$ s/mm^2 (or, equivalently, 3 ms/μm^2), but it becomes inadequate at higher b values ($b > 3000$ s/mm^2), where it fails to capture the observed signal decay (McKinnon et al., 2017; Palombo et al., 2018).

The SANDI model (Palombo et al., 2020) addresses this limitation by incorporating a third diffusive compartment, which accounts for the unmodeled contribution of soma within GM. The SANDI model builds on the assumptions of the SM and experimental evidence suggesting that, at short diffusion times t_d (t_d<20 ms given a water bulk diffusivity of ~3 μm^2/ms and an estimated pre-exchange time >500 ms), the effects of cell membrane permeability and water exchange between intra-cellular and extra-cellular spaces are negligible (Yang et al., 2018). Additionally, this model assumes, as tested through numerical simulations (Palombo et al., 2020) that, at these short t_d, the intracellular sub-compartments, i.e. soma and neurites, can be treated as separate, non-exchanging compartments.

According to the SANDI model, the signal attenuation from the DW-MRI experiment as a function of b-value (S(b)), normalized to the image without diffusion weighting, (S(0)) is:

$$\frac{S(b)}{S(0)} = f_{ic}\left(f_{in}A_{in}(b) + f_{is}A_{is}(b)\right) + f_{ec}A_{ec}(b) \quad (1)$$

where f_{ic} and f_{ec} are the intra-cellular and extra-cellular relative signal fractions (for which the condition $f_{ic} + f_{ec} = 1$ is always valid), f_{in} and f_{is} are the intra-neurite and intra-soma relative signal fractions (for which the condition $f_{in} + f_{is} = 1$ is always verified), A_{in} and A_{is}, A_{ec} are the normalized signals of the neurites, soma and extra-cellular space, respectively. To obtain orientationally independent diffusion metrics, the powder-averaged signal (that is, the average of the signal across various uniformly distributed directions) can be considered. The normalized, direction-averaged signal is indicated by $\widetilde{\frac{S(b)}{S(0)}}$, comprising $\widetilde{A}_{in}$ and $\widetilde{A}_{is}$, $\widetilde{A}_{ec}$, detailed below.

For the *extra-cellular compartment* or space, $\widetilde{A}_{ec}(b, D_{ec})$ depends on the b-value and the extra-cellular diffusivity (D_{ec}, from now on simply named D_e) and can be expressed, assuming isotropic Gaussian diffusion in this compartment, as:

$$\widetilde{A}_{ec}(b, D_e) \approx e^{-bD_e} \quad (2)$$

Table 1
Overview of parameters for Diffusion - Weighted Imaging (DWI) and R1 protocols.

Parameter	DWI Protocol	R1 mapping Protocol
Total DWI Volumes	266	–
Diffusion Directions/ Volumes per b-shell	13 / 20 / 20 / 30 / 61 / 61 / 61	–
Diffusion Weightings (b-values)	0 / 200 / 500 / 1200 / 2400 / 4000 / 6000 s/mm^2	–
Acquisition Method	Double-refocused spin-echo DW echo-planar imaging	MP2RAGE
Repetition Time (TR)	3000 ms	5000 ms
Echo Time (TE)	85 ms	2.36 ms
Flip Angle (FA)	50°	FA1 = 7°, FA2 = 5°
Refocusing Flip Angle	180°	–
Diffusion Gradient Separation (Δ)	40 ms	–
Diffusion Gradient Duration (δ)	28 ms	–
Resolution	2.5-mm isotropic	1-mm isotropic
Number of Slices	42	160
Field of View (FOV)	220 × 220 mm^2	224 × 224 mm^2
Bandwidth	1496 Hz/pixel	350 Hz/pixel
GRAPPA Acceleration	2	2
Inversion Times (TI)	–	TI1=700 ms, TI2=1500 ms
Echo Spacing	0.75 ms	5.8 ms
Slice orientation	Transversal	Sagittal
Scan duration	13.48 min	7.55 min

GRAPPA=GeneRalized Autocalibrating Partial Parallel Acquisition; DW=diffusion weighted; MP2RAGE= Magnetization Prepared 2 Rapid Acquisition Gradient Echoes.

For the *intra-neurite compartment*, $\widetilde{A}_{in}(b, D_{in})$ depends on the b-value and the axial intra-neurite diffusivity (D_{in}), which describes the diffusion of water along the length of neurites, modeled as randomly oriented cylinders or sticks with negligible radial diffusivity ($D_{\perp}\approx 0$). The normalized signal from neurite diffusion is thus:

$$\widetilde{A}_{in}(b, D_{in}) \approx \sqrt{\frac{\pi}{4bD_{in}}}\mathrm{erf}\left(\sqrt{bD_{in}}\right) \tag{3}$$

Finally, for the intra-soma compartments, $\widetilde{A}_{is}(b, D_{is}, r_s)$ depends not only on the b-value, the intra-soma diffusivity (D_{is}) and the cellular size (r_s) but also on additional parameters such as the diffusion gradient amplitude (g), the gradient pulse duration (δ), and the time between the gradient pulses (Δ). It represents the normalized signal arising from diffusion within somas, which are modeled as spheres:

$$\widetilde{A}_{is}(b, D_{is}, r_s) \approx exp\left\{ -\frac{2(\gamma g)^2}{D_{is}} \sum_{m=1}^{\infty} \frac{a_m^{-4}}{a_m^2 r_s^2 - 2} \times \left[2\delta - \frac{2 + e^{-a_m^2 D_{is}(\Delta-\delta)} - 2e^{-a_m^2 D_{is}\delta} - 2e^{-a_m^2 D_{is}\Delta} + e^{-a_m^2 D_{is}(\Delta+\delta))}}{a_m^2 D_{is}} \right] \right\} \tag{4}$$

where γ is the gyromagnetic ratio, a_m is the root of a Bessel function-related equation, and r_s quantifies the radius or apparent soma size. The parameter D_{is} characterizes water diffusion inside somas (for practical applications, D_{is} is often set to the self-diffusion coefficient of water at tissue temperature).

By substituting Eqs. (2), (3) and (4) into Eq. (1), we get the approximated expression for the total direction-averaged signal:

$$\frac{\widetilde{S}(b)}{S(0)} = (1 - f_{ec})(f_{in}\widetilde{A}_{in}(b, D_{in}) + (1 - f_{in})\widetilde{A}_{is}(b, D_{is}, r_s)) + f_{ec}\widetilde{A}_{ec}(b, D_e) \tag{5}$$

The parameters to be estimated fitting the DW-MRI signal to Eq. (5) are five in total, as D_{is} is set to a fixed value of 3 μm^2/ms (corresponding to 3 × 10^{-3} mm^2/s), corroborated by numerical simulations and Pulsed Gradient Spin Echo experiments (Palombo et al., 2020), while fextra (the extra-cellular intensity fraction) is equal to fextra=1-fsoma-fneurite (with fsoma equivalent to $(1\text{-}f_{ec})(1\text{-}f_{in})$ in Eq.(5), and fneurite equivalent to $(1\text{-}f_{ec})f_{in}$ in Eq.(5)).

2.2. Data acquisition

2.2.1. Participants

The study participants were 20 healthy adult volunteers (9 males and 11 females). The age range was 24 – 31 years (mean = 27.5 years; standard deviation (SD) = 3.8 years). Participants provided written informed consent, and they were screened for MRI compatibility. None of the subjects had a history of neurological disease, psychological disorders, drug or alcohol abuse, or use of neuropsychiatric medication. Participants were instructed to maintain their usual intake of food, drink (including alcohol), and caffeine on the day of the study. The study was approved by the Cardiff University School of Psychology Ethics Committee.

2.2.2. MRI protocol

The imaging protocol was conducted on a Siemens Prisma 3T scanner (Siemens Healthineers, Erlangen, Germany) at the Cardiff University Brain Research Imaging Centre (CUBRIC), using a 32-channel, receive-only head coil. All participants underwent a protocol including diffusion-weighted imaging (DWI) with varying gradient strengths and quantitative R1 mapping via Magnetization Prepared 2 Rapid Acquisition Gradient Echo (MP2RAGE) sequence (Marques et al., 2010), with detailed sequence parameters listed in Table 1. The MP2RAGE sequence models R1 assuming that water exchange between free water and water bound to macromolecules is negligible, and that each voxel comprises a single spin pool of water molecules, whose signal recovery after excitation can be theoretically described by a mono-exponential behavior.

DWI included six non-zero b-shells with increasing diffusion directions at higher b-values and 13 b0 volumes acquired with phase-encoding in an anterior-posterior direction. In addition, an image with no diffusion weighting but an opposite phase-encoding direction was acquired for susceptibility distortion correction. B-value shuffling was adopted to avoid excessive gradient coil heating (Hutter et al., 2018).

2.3. Data processing and statistics

Diffusion weighted images (DWIs) were denoised (Veraart et al., 2016) and corrected for Gibbs ringing artifacts with MRtrix3 (Tournier et al., 2019). The b0-images acquired in opposite phase encodings were used to estimate the susceptibility induced distortions via FSL TOPUP (FSL, FMRIB Software Library, v6.0.1 (Jenkinson et al., 2012)). FSL BET was used to provide a binary mask to FSL EDDY, which was employed to correct for eddy-current induced distortions and subject motion, exploiting the output from TOPUP. Diffusion data quality check was conducted via the evaluation of the signal-to noise ratio, using in-house MATLAB scripts (MATLAB version: R2022b, Natick, Massachusetts: The MathWorks Inc). MATLAB was also used to derive a map of apparent R1 (apparent due to the single compartment assumption; thereafter, simply named R1) from the quantitative T1 map produced by the MP2RAGE sequence, and for the correlation analysis, detailed below. FSL DTIFIT

was used to extract the diffusion tensor using b-values up to 1200 s/mm^2, yielding mean diffusivity and fractional anisotropy (FA) maps, and the tensor eigenvalues and eigenvectors. FA maps were later used for parcellation of white and gray matter.

The SANDI toolbox (https://github.com/palombom/SANDI-Matlab-Toolbox-Latest-Release) was used to estimate via a Machine Learning approach based on Random Forest Regression, five model parameters: *fsoma* (equivalent to $(1-f_{ec})(1-f_{in})$ in Eq.(5)), *fneurite* (equivalent to $(1-f_{ec})f_{in}$ in Eq.(5)), the signal fractions of intra-soma and intra-neurite compartments (the extra-neurite signal fraction *fextra* was computed from them as *fextra*=1-*fsoma*-*fneurite* and corresponds to f_{ec} in Eq. (5)); D_{in}, D_e, the apparent diffusivities of intra-neurite and extra-neurite compartments, respectively; *Rsoma* (r_s), the estimated magnetic resonance (MR) apparent radius of soma and/or cellular bodies (e.g. glia).

2.3.1. Signal to noise ratio of DWIs

A critical aspect to consider when analyzing DWI data is the reliability of the acquired signal. Indeed, noise can introduce bias into the estimated diffusion metrics (Jones and Basser, 2004). To ensure robust data quality, the signal-to-noise ratio (SNR) of the DW images was evaluated. Conventionally, SNR is evaluated for each diffusion-encoded volume and thus, each b-value, allowing to verify whether the measured signal falls below the noise floor at the highest b-value (Caporale et al., 2017). SNR is calculated as the ratio between the diffusion signal in WM and GM and the standard deviation of the noise in the background. This approach (hereafter referred to simply as SNR) provides an overall measure of signal reliability across the dataset. To this aim, the SNR averaged across subjects for each diffusion direction was calculated. However, because of the use of parallel imaging and a multi-channel receiver head coil, SNR was evaluated also following the definition proposed by Dietrich et al. (2007) (Dietrich et al., 2007), employing two raw, uncorrected images without diffusion weighting, or $b = 0$ s/mm^2 images. Because the method considers the difference between two consecutive b0 images, it will be referred to as SNR_{diff} hereafter. The SNR_{diff} was thus defined as:

$$SNR_{diff} = \frac{1}{\sqrt{2}} \frac{mean_{ROI}(S_1(b=0) + S_2(b=0))}{std_{ROI}(S_1(b=0) - S_2(b=0))} \quad (6)$$

where $S_1(b = 0)$ and $S_2(b = 0)$ represent the signal in the first two consecutive $b = 0$ s/mm^2 images acquired. The two SNRs were calculated in two regions of interest (ROIs), namely the WM and GM, and were reported as the mean ± standard deviation. The corpus callosum was chosen because, due to the presence of highly coherent WM fibers, it represents a region where the diffusion is highly facilitated along the fiber direction (corresponding roughly to the left-right direction) and highly hindered in the perpendicular direction. Therefore, the direction of facilitated diffusion may represent the worst-case scenario in the SNR evaluation due to larger signal attenuation.

The FA maps were used to mask the corpus callosum for SNR evaluation and normalization of the parametric maps to the standard Monreal Neurological Institute (MNI) space. For SNR calculation, the corpus callosum was selected in an automated way, by retaining voxels with FA larger than 0.75 and with the first eigenvector (V1) magnitude larger than 0.9 to allow the selection of coherent WM fibers and to avoid partial volume effects at the borders. For the same reason, GM was selected in an automated way by retaining voxels with FA comprised between 0.15 and 0.38. These thresholds were set empirically considering the average FA and V1 values in the respective tissues of interest (the corpus callosum and GM) and were applied only for SNR evaluation purposes. Noise was evaluated in the background by automatically selecting four squares at the corners of the image (size of the square was roughly 1/5 of the matrix size). The code is available at https://github.com/caporaleas/SNR_DWI.

2.3.2. Parametric maps normalization and white and gray matter parcellation

The FA map was registered to the anatomical T1-weighted image via rigid body transformation. The structural image was normalized to the MNI-2-mm space via non-linear transformation. These transformations were combined to obtain the warps that mapped the FA onto the MNI standard space, and the warps were applied to the R1 and SANDI parametric maps. A hard segmentation of the T1-image was used based on the absolute maximum partial volume estimate, obtaining masks of GM and WM, which were further eroded. For cortical parcellation, the Human Connectome Project (HCP) atlas, including 180 regions of interest (ROIs) (Glasser et al., 2016), was used. In this atlas information related to the architecture, topography, function and connectivity of the GM areas were used to obtain the cortical parcellation. The analysis was restricted to cortical gray matter (GM) due to the atlas chosen for cortical parcellation. In the **Supplementary Materials** we reported the results of an analysis including also subcortical structures. The ICBM-DTI-81 (Mori et al., 2008) atlas, including 50 ROIs, was used instead for WM parcellation. GM and WM ROIs exceeding the 20th percentile in voxel count were retained to exclude residual noise. Voxels with cell density (*fsoma*) higher than 0.1 were retained ensuring brain parenchyma selection and a reliable estimate of Rsoma in the parenchyma (Afzali et al., 2021).

2.3.3. Statistical analysis

The median regional values of SANDI and parametric maps of R1 were evaluated across subjects and across ROIs, with standard deviations and errors. Pearson's correlation was evaluated between the regional values of R1 and SANDI metrics, correcting for multiple comparisons (using Benjamini-Hochberg false discovery rate criterion, thereafter, simply named FDR). The distribution of correlation coefficients was also evaluated across subjects. In the correlation between SANDI metrics and R1 across ROIs the effect of several potential confounders (ROI volume, the cortical thickness and curvature for GM, and ROI volume only for WM) was evaluated. The ROI volume was expressed as the number of voxels constituting the GM or WM ROI. The cortical thickness and the curvature were estimated using FreeSurfer (FreeSurfer (Fischl, 2012), v7.3.2) for each ROI of the HCP atlas, considering then the median across subjects. A regression analysis was performed using the 'General Linear Model' (fitglm) in MATLAB, and employing standardized variables. The model tested for the GM ROIs was the following:

$$SANDImetric_i = \beta_0 + \beta_1 \cdot R1_i + \beta_2 \cdot C1_i + \beta_3 \cdot C2_i + \beta_4 \cdot C3_i + \varepsilon_i \quad (7)$$

Where C1, C2 and C3 were the ROI volume, the cortical thickness and the curvature, respectively. The model tested for the WM ROIs included a single confounding factor, the ROI volume:

$$SANDImetric_i = \beta_0 + \beta_1 \cdot R1_i + \beta_2 \cdot C1_i + \varepsilon_i \quad (8)$$

A conservative p-value of p'=0.05/6 = 0.0083, with 6 the number of SANDI metrics was considered as statistically significant, to control for the family-wise error rate.

Mean values ± standard deviations of R1 and SANDI metrics were evaluated in GM and WM without any threshold, using the binarized partial volume estimate maps, to enable comparison with other studies. The code is available at https://github.com/caporaleas/STR_CORR.

3. Results

No subject was excluded due to severe movement or ringing artifacts, leading to a dataset of 20 healthy subjects.

The calculated mean SNR_{diff} values were 28.56 ± 5.11 for GM and 29.77 ± 4.01 for WM, indicating a comparable level of data quality across both tissue types and to recent studies in healthy subjects at 3T (Schiavi et al., 2023). The conventional SNR evaluated in the corpus callosum (CC) and in the GM for each b-value is shown in Fig. 1. The across-subject average was calculated for each distinct diffusion

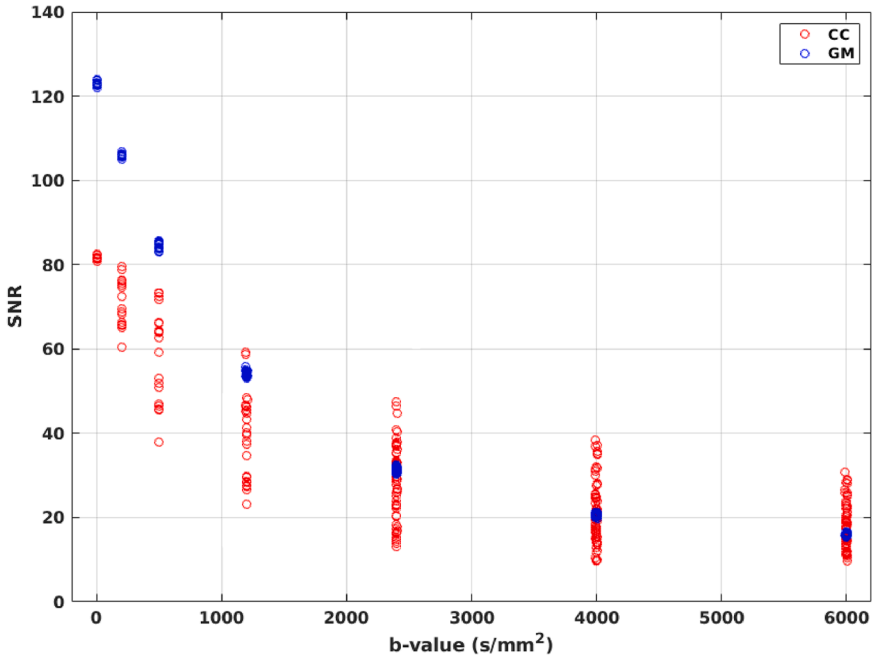

Fig. 1. Signal-to-noise ratio (SNR) of diffusion-weighted images. The SNR evaluated for each diffusion volume (averaged across subjects) is plotted against the b-values for the corpus callosum and gray matter (CC and GM, shown in red and blue, respectively). Experimental points represent the mean SNR across subjects.

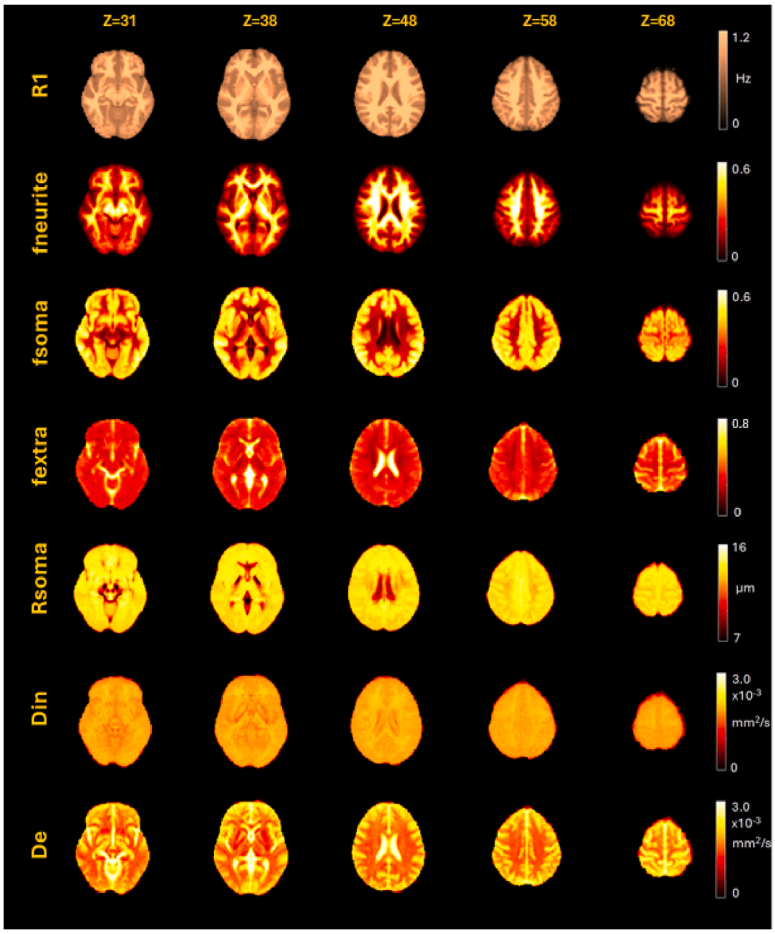

Fig. 2. Group average parametric maps. Parametric maps of R1 and SANDI metrics normalized to MNI space and averaged across all subjects. R1 = 1/T1, relaxation rate; fneurite = signal intensity fraction of neurite compartment; fsoma = signal intensity fraction of cellular compartment; fextra = signal intensity fraction of extra-cellular compartment; Rsoma = average size of cellular bodies; D_{in} = diffusivity of the intra-neurite compartment; D_e = diffusivity of the extra-neurite compartment. The different slices correspond to axial sections at different Z-coordinates (Z = 31, 38, 48, 58, 68) in MNI space.

direction. Notice the spread of SNR values in the CC (and not in the GM) due to the inhomogeneous diffusion attenuation depending on the diffusion sensitizing gradient direction. This is caused by the directionality of the diffusion phenomenon in WM. Even for the diffusion direction with the highest signal attenuation (that is [1 0 0], corresponding to the orientation of the most coherent fibers in the corpus callosum) the SNR remains above the inferior limit allowed for the reliability of DW data (SNR=3), according to Jones et al. (Jones et al., 2013).

Parametric maps of R1 and SANDI metrics obtained in the current study, normalized to the standard MNI space and averaged across subjects are shown in Fig. 2. The intensity fractions of the three diffusive compartments (neurites, cellular bodies or soma, and extra-cellular space) are shown, together with the quantitative maps of average soma size, and the diffusivities of the intra-neurite and extra-neurite domains.

R1 ranged between a value of 0.77 ± 0.02 s^{-1} to 1.11 ± 0.03 s^{-1} in GM and WM, respectively. On average, GM presented signal fractions of the soma, extra-neurite and intra-neurite compartments of 0.41 ± 0.01, 0.36 ± 0.01 and 0.19 ± 0.01, respectively. On average, in WM the largest signal fraction originated from the neurite compartment (fneurite=0.41 ± 0.02), followed by the signal fraction of the extra-neurite and the soma water pools (0.31 ± 0.01 and 0.27 ± 0.01, respectively). The estimated soma radius showed minimal differences between GM and WM (Rsoma=13.00 ± 0.14 in GM and 13.08 ± 0.17 μm in WM). Regarding diffusivity measures, the intra-neurite diffusivity (D_{in}) was 1.75 ± 0.02 $\mu m^2/ms$ in GM and 1.87 ± 0.02 $\mu m^2/ms$ in WM, while the extra-neurite diffusivity (D_e) was 1.90 ± 0.06 $\mu m^2/ms$ in GM and 1.64 ± 0.06 $\mu m^2/ms$ in WM.

Scatter plots of R1 and SANDI metrics across ROIs are shown in Fig. 3. Since R1 presents different ranges of values for GM and WM, the correlation plots for these two tissue types were illustrated separately. For each ROI, the marker indicates the median value of the SANDI metrics across subjects for that ROI, plotted against the median value of R1 across subjects. Correlation analyses revealed a moderate negative association between R1 and soma-related parameters in GM ROIs, with R1 negatively correlated with fsoma (r = -0.51, $p < 0.0001$) and Rsoma (r = -0.47, $p < 0.0001$). Additionally, R1 showed a positive correlation with fextra and D_e (r = 0.38, $p < 0.0001$) but only a weak association with neurite density (fneurite, with r = 0.18, FDR-adjusted p = 0.028, data not shown) while no significant relationship was found with neurite diffusivity (D_{in}). The scatter plots of the SANDI parameters and R1 across ROIs including the subcortical structures are shown in the **Supplementary Materials**. The inclusion of the subcortical structures increased the entity of the correlation between the signal fraction of soma and neurite compartments (fneurite, fsoma) and R1. In particular, the correlation between fneurite and R1 became statistically significant with the inclusion of the subcortical structures. On the other hand, the correlation between Rsoma and R1 decreased.

Within WM ROIs, moderate to strong positive correlations were observed between R1 and intra-neurite metrics, with D_{in} (r = 0.62, $p <$ 0.0001) and fneurite (r = 0.43, FDR-adjusted p = 0.019. The ROI volume was not related to R1 in GM (r = 0.05 and p = 0.52, **Supplementary Materials, Figure S4a**) but it was related with R1 in WM (r = 0.47, p = 0.002). The cortical thickness was not related to R1 in GM (r = -0.08, p = 0.32, **Figure S4b**), and the curvature was weakly related to R1 in GM (r = 0.17, p = 0.046, **Figure S4c**). The estimated beta coefficients of the regression analysis with the respective p-values are reported in Table 2. For the WM only the fneurite and D_{in} were included as dependent variables because the other diffusion metrics did not show a significant correlation with R1 in the original analysis. A significant p-value of the β_1 coefficient indicates that there is a linear relationship between the specific diffusion metric and R1 that is not explained by the confounding factors included in the model. In the GM, the correlations between fsoma and R1, fextra and R1, Rsoma and R1 and D_e and R1 remained significant after including the confounding factors. In the WM, the correlation between fneurite and R1 was not significant after including the ROI volume but the correlation between the intra-neurite diffusivity (D_{in}) and R1 remained significant.

The subject-wise spatial correlation coefficient between SANDI

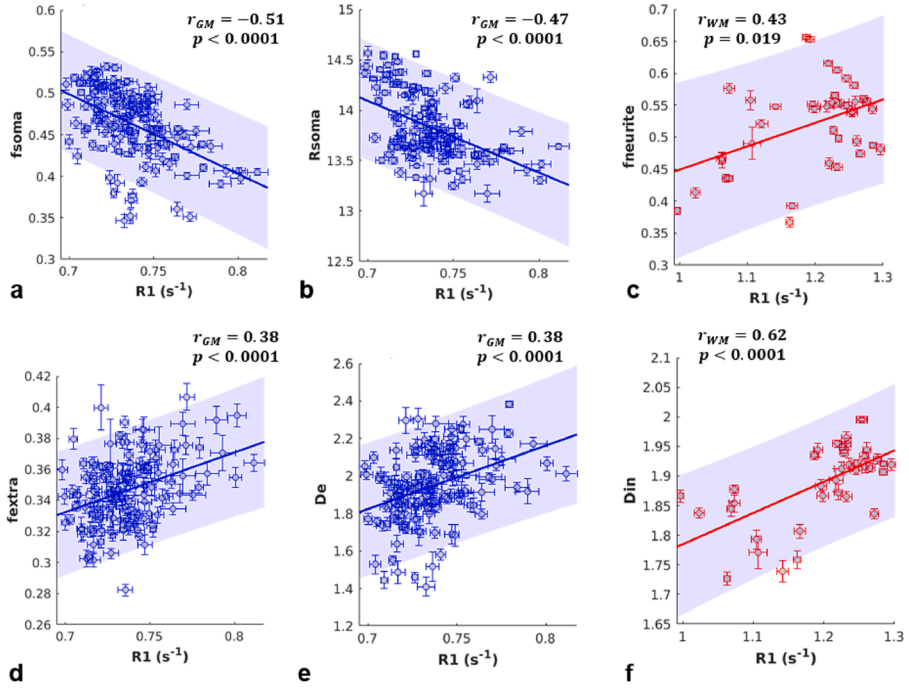

Fig. 3. Scatter plots of SANDI metrics vs R1 in Gray and White Matter regions (GM and WM, respectively). The Pearson's correlation coefficient between R1 and SANDI metrics quantified in GM and WM regions is indicated (with FDR-adjusted p-values shown). Each marker represents, for a different brain region, the median across subjects of the regional median of the parameter. Error bars are standard errors (median absolute deviations/squared root of number of subjects). Markers and regression lines are shown in blue and red for GM and WM, respectively. Shaded areas represent 95 % confidence intervals.

Table 2
Beta coefficients of the regression analysis performed in GM considering the model in Eq. 7 and in WM considering the model in Eq. 8. The respective p-value is indicated in parentheses.

	SANDI metric	β_0 (intercept)	β_1 (R1)	β_2 (ROI volume)	β_3 (cortical thickness)	β_4 (curvature)
GM	**fneurite**	0.0088 (0.92)	0.19 (0.024)	−0.0081 (0.92)	0.14 (0.087)	−0.028 (0.75)
	fsoma	0.0042 (0.96)	**−0.47 (<0.0001)**	−0.039 (0.61)	−0.14 (0.056)	0.050 (0.53)
	fextra	−0.010 (0.89)	**0.39 (<0.0001)**	0.0032 (0.97)	0.11 (0.16)	−0.026 (0.75)
	Rsoma	0.0061 (0.94)	**−0.35 (<0.0001)**	−0.10 (0.19)	0.13 (0.09)	−0.027 (0.75)
	Din	0.0072 (0.93)	−0.097 (0.26)	−0.012 (0.89)	0.019 (0.83)	0.035 (0.70)
	Dextra	−0.0076 (0.92)	**0.42 (<0.0001)**	0.054 (0.49)	−0.11 (0.14)	−0.061 (0.45)
WM	**fneurite**	<0.0001 (1)	0.30 (0.069)	0.27 (0.098)	–	–
	Din	<0.0001 (1)	**0.53 (0.0003)**	0.27 (0.052)	–	–

fneurite=signal fraction of the neurite compartment; fsoma=signal fraction of the soma compartment; fextra=signal fraction of the extra-neurite compartment; Rsoma=average size of cellular bodies; Din=intra-neurite diffusivity; De=extra-neurite diffusivity; GM=gray matter; WM=white matter.

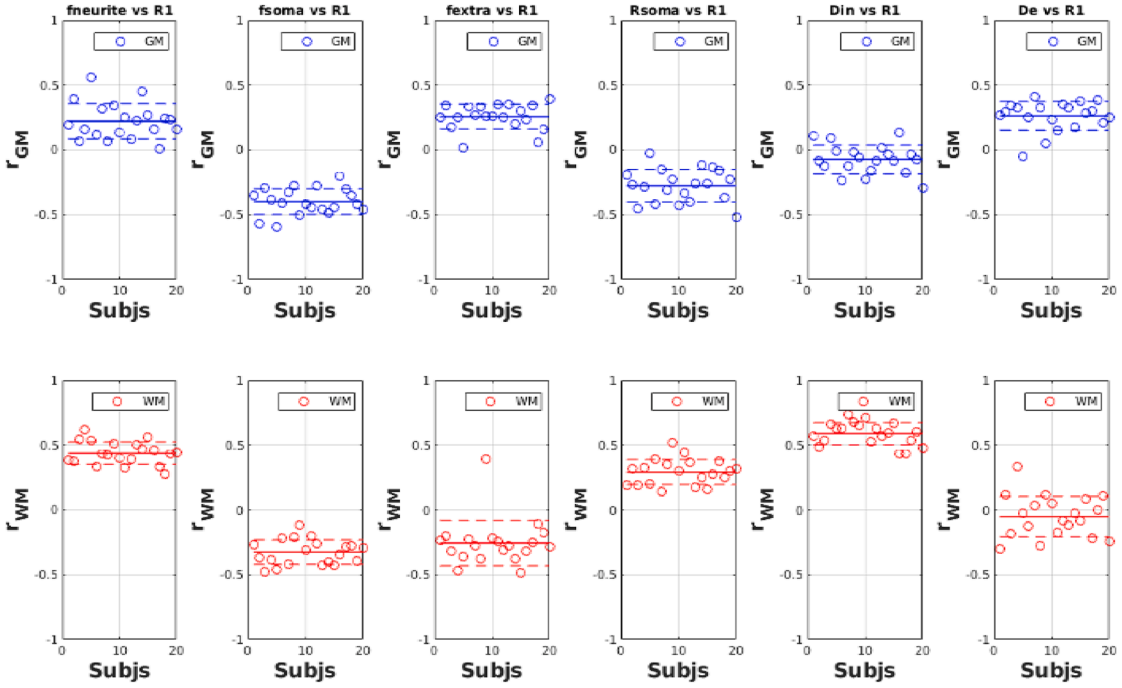

Fig. 4. Subject-wise correlation coefficient between SANDI metrics and R1. Each marker represents the correlation coefficient between SANDI metrics and R1 in the Gray Matter (GM) or White Matter (WM) regions, for each subject. The grand mean ± standard deviation of r are indicated by the thick and dashed lines, respectively.

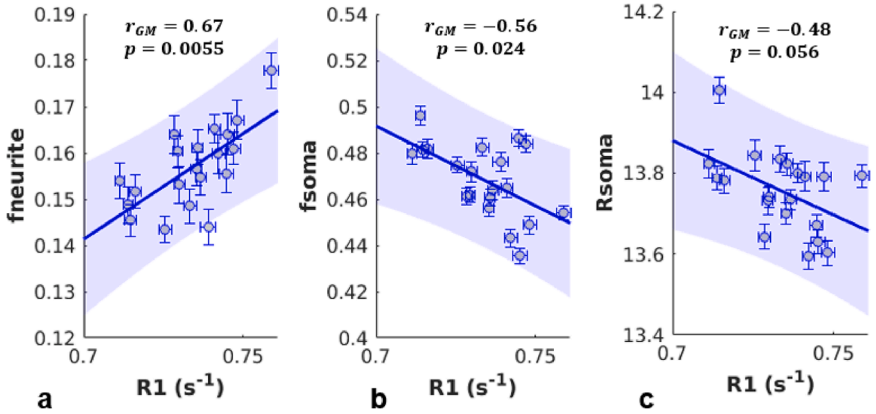

Fig. 5. Scatter plots of SANDI metrics vs R1 in Gray Matter across subjects. The Pearson's correlation coefficient between SANDI metrics quantified in GM regions is indicated (with FDR-adjusted p-values shown). Each marker represents, for a different subject, the median across regions of the specific parameter. Error bars are standard errors (median absolute deviations/squared root of number of subjects). Markers and regression lines are shown in blue. Shaded areas represent 95 % confidence intervals.

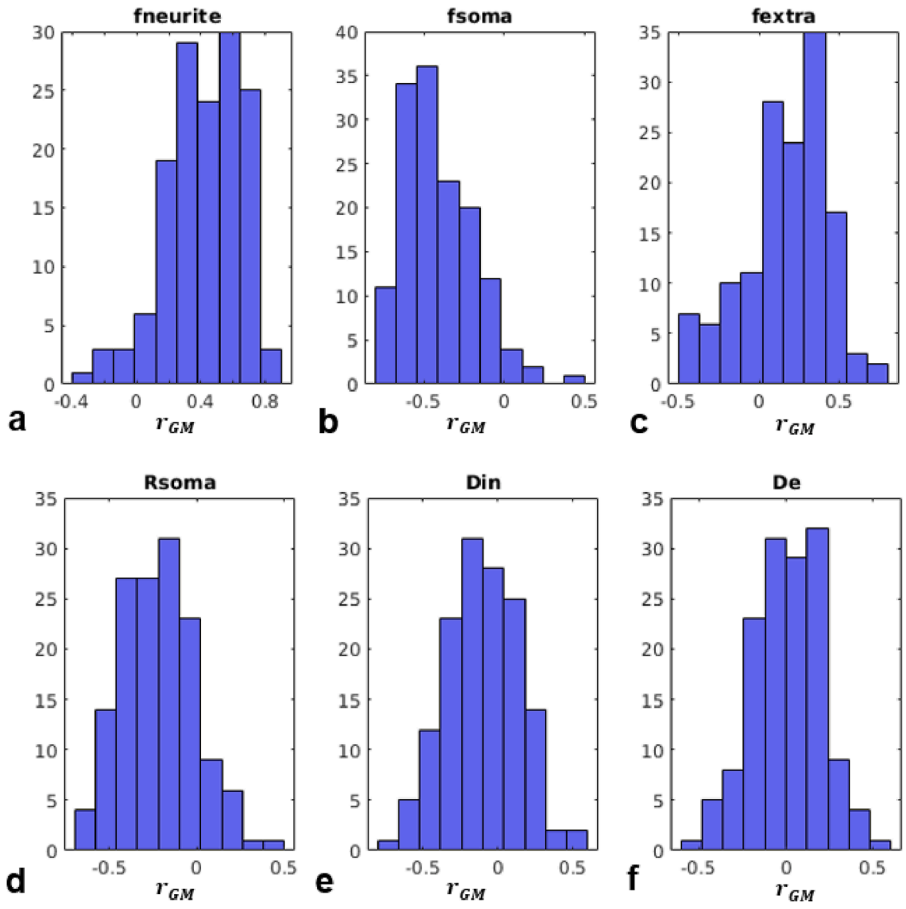

Fig. 6. Distribution of correlation coefficients between SANDI metrics and R1 across subjects for various Gray Matter regions (ROIs). Histograms of the Pearson's correlation coefficients between R1 and SANDI metrics across-subjects, for each gray matter ROI.

metrics and R1 in both GM and WM is illustrated in Fig. 4. Including the subcortical structures did not affect significantly the results of the correlations between SANDI metrics and R1 across subjects, as shown in **Figure S**3. The scatter plots of global GM R1 and SANDI metrics across subjects are shown in Fig. 5. Each marker represents the median across regions of a given parameter for a different subject. A positive correlation was observed between fneurite and R1 ($r = 0.67$, FDR-adjusted $p = 0.0056$), while fsoma and R1 exhibited a negative correlation ($r = -0.56$, FDR-adjusted $p = 0.024$). Additionally, a negative trend was noted between Rsoma and R1 ($r = -0.48$, FDR-adjusted $p = 0.056$). The distributions of correlation coefficients between R1 and SANDI metrics across subjects, for each gray matter ROI, are shown in Fig. 6.

4. Discussion

In this study, we tested the hypothesis that the GM microstructural characteristics, specifically its cytoarchitecture, contributed to R1 contrast, determining associations between SANDI-derived diffusion metrics in GM and R1 in healthy subjects. R1 was derived using the MP2RAGE sequence, based on a mono-compartmental model of longitudinal magnetization recovery. The findings revealed distinct associations between microstructural properties and R1 in GM and WM, providing complementary insights into cortical organization.

4.1. Diffusion data metrics and R1 mapping

Given that the diffusion protocol included b-values larger than 3000 s/mm^2, an assessment of data reliability was necessary. The evaluation of SNR confirmed that the signal remained above the noise floor, and the SNR_{diff} in the image without diffusion weighting was reasonable and comparable to a previous study evaluating SANDI metrics in healthy adults using the same clinical 3T scanner model (Schiavi et al., 2023).

Overall, the R1 values measured in this study aligned well with published benchmarks for healthy individuals at 3T, supporting the robustness of R1 mapping. In WM, R1 averaged 1.11 ± 0.03 s^{-1}, in agreement with previously reported ranges (Berg et al., 2022; Weiskopf et al., 2013) In GM, R1 averaged 0.77 ± 0.02 s^{-1}, in agreement with the values reported by Marques et al. (Marques et al., 2010) but (slightly exceeding the reported range of 0.61 - 0.75 s^{-1} (Berg et al., 2022; Weiskopf et al., 2013). This deviation may reflect methodological differences, such as variations in MRI acquisition protocols, segmentation techniques, or demographic characteristics of the studied cohort.

Overall, some of the SANDI metrics were comparable with the literature, while others were not. The average extracellular signal fraction (fextra) measured in this study was 0.36 ± 0.01 in GM and 0.31 ± 0.01 in WM, which are consistent with the literature: for instance, Schiavi et al. (Schiavi et al., 2023) observed fextra values of 0.40 in GM and 0.30 in WM, while Krijnen et al. (Krijnen et al., 2023) reported fextra values ranging from 0.23 - 0.52 in GM and 0.15 - 0.46 in normal-appearing WM, for diffusion times $\Delta = 19$ and $\Delta = 49$ ms, respectively. Similarly, the average neurite signal fraction (fneurite) measured in this study was 0.19 ± 0.01 in GM and 0.41 ± 0.02 in WM. These values fall well within the range reported by (Krijnen et al., 2023; Schiavi et al., 2023) for healthy individuals. The soma signal fraction (fsoma) measured in this study was 0.41 ± 0.01 in GM and 0.27 ± 0.01 in WM. These values are higher than those reported by (Schiavi et al., 2023), who observed fsoma values of approximately 0.27 in GM and 0.15 in WM, and align more closely with the findings of Krijnen et al.

(Krijnen et al., 2023), who reported fsoma values of 0.55 and 0.33 in GM (averaged across cortical and deep GM) and 0.43 and 0.26 in normal-appearing WM of healthy controls, for diffusion times $\Delta = 19$ and $\Delta = 49$ ms, respectively. The soma radius (Rsoma) measured in this study was 13.00 ± 0.14 μm in GM and 13.08 ± 0.17 μm in WM exceeding the range reported by (Krijnen et al., 2023; Schiavi et al., 2023). Schiavi et al. observed Rsoma values of 12.68 μm in GM and of 10.02 μm in WM, while Krijnen et al., reported Rsoma values of 10.10 in GM and 10.23 - 10.33 in normal - appearing WM for diffusion times $\Delta = 19$ and $\Delta = 49$ ms, respectively. The small difference in Rsoma between GM and WM in the present study could reflect the insensitivity of the diffusion protocol to true compartment differences, rather than a biologically meaningful similarity. This would affect particularly WM estimates, where cell body density (fsoma) is lower and the axonal components dominate the diffusion signal. Finally, the intra- and extra-neurite diffusivities (D_{in} and D_e, respectively) measured in this study were respectively underestimated and overestimated by approximately 30–35 % with respect to (Schiavi et al., 2023) while (Krijnen et al., 2023) did not provide explicit D_{in} and D_e values, limiting a direct comparison.

When comparing the SANDI-derived diffusion metrics obtained in this study for GM and WM with values reported in literature for healthy subjects, we must consider that: first, the diffusion time employed (given by $\Delta - \delta/3$, with Δ diffusion gradient separation and δ diffusion gradient duration, which in our case is roughly 31 ms) modulates the sensitivity of the diffusion sequence to inter-compartmental water exchange; second, the values yielded by the multi-parametric fitting of diffusion data at different gradient strengths were obtained by fixing the intra-soma diffusivity (D_{is}) to a value of 3 μm^2/ms, without directly constraining the upper bound in the fit; third, methodological differences in the data acquisition (e.g., the number and arrangement of b-shells) and analysis (e.g., the fitting algorithm used to extract the SANDI metrics) potentially affect the estimation of the diffusion metrics. Due to the first point, the diffusion time employed in the sequence slightly influences the estimated fraction of the three diffusive compartments. Regarding the second point, simulations and in vitro experiments have shown that the fitting remains stable across a wide range of D_{is} values, from 0.1 to 3 μm^2/ms, with only minimal variations in the estimated parameters (Palombo et al., 2020). Finally, regarding the third point, the discrepancies in parameter estimates can arise first of all from the use of different b-values in the diffusion protocol. Indeed, while Schiavi et al.'s protocol employed 0/500/1000/2000/3000/4000/6000 s/mm^2, our protocol included a b-value of 200 s/mm^2, but did not include a b-value of 3000 s/mm^2. Future studies regarding the impact of adding more b-values between 200 and 1000 s/mm^2 are warranted. Another source of difference between our results and those reported in Schiavi's and Krijnen's studies lies in the fitting approach. While we used a machine learning non-linear fitting, the other two studies employed a linearized and heavily regularized version of the fitting using the AMICO framework. This difference in methodology can lead to slightly different parameter estimates.

4.2. Associations between R1 and diffusion-derived metrics

The associations between R1 and SANDI metrics could be confounded by some macroscopic tissue characteristics, such as cortical thickness, the volume of the region, water content and iron content contributing to R1 contrast (the latter two were not quantified in the present study). Although the use of median values in the ROI is less sensitive to outliers and therefore more robust to 'noise', it is important to take into account the potential confounding factors in the correlation analysis. In GM, across ROIs, a significant negative correlation was observed between R1 and soma-related metrics, with lower R1 values corresponding to higher fsoma and larger soma radii (Rsoma), as depicted in Fig. 3. These results were significant even when controlling for GM ROI volume, cortical thickness and curvature (Table 2).

We can only speculate that these findings suggest that less myelinated regions tend to harbor larger neuronal somas, and that this may reflect differences in network functionality across cortical areas (Turner, 2019). A potential link to learning remains thus only a hypothesis that requires further investigation. In this hypothetical view, such a relationship may represent a functional adaptation, where cortical areas with lower myelination maintain larger somas to support higher metabolic demands and synaptic plasticity. Such structural variations across the cortex could contribute to differential processing and learning capacities in different brain regions, underscoring the potential role of GM myelination in facilitating neuroplasticity, as regions with varying myelination levels may exhibit different capacities for adaptation and learning. The association between larger neuron sizes and lower myelination (assuming that the measured R1 depends on myelin content, among other factors) may suggest that specific cortical regions are structurally optimized for distinct functional roles, potentially influencing how information is processed within the brain. In this way, the variability in GM myelination across the human cortex could be pivotal in supporting complex cognitive functions (Call and Bergles, 2021; Dicke and Roth, 2016). These explanations remain, however, speculative. Another possible reason why more densely myelinated regions would present smaller soma density and soma size could be linked to regional differences in cell type composition that may also influence soma size estimates. Indeed, the smaller size of oligodendrocyte cell bodies densely packed in the voxel would decrease the 'apparent' Rsoma measured with MRI (which represents a volume weighted mean of the cell sizes within a given voxel).

Moreover, considering the median across ROIs and the correlation across subjects, a positive correlation was observed between fneurite and R1 (r = 0.67, FDR-adjusted p = 0.0056), while fsoma and R1 exhibited a negative correlation (r = -0.56, FDR-adjusted p = 0.024). These results indicate that individuals with higher global R1 in GM also exhibit a higher intensity fraction of neurites, and a lower intensity fractions of somas, which is in line with the fact that R1 depends, among other factors, on the myelin content (and the intensity fraction of neurites is proportional to the density of myelinated fibers), and suggests that myelination patterns in the cortex are influenced by different neuron intrinsic factors, other than the size, such as neuronal identity, as shown in literature (Call and Bergles, 2021). Additionally, a negative trend was noted between Rsoma and R1 (r = -0.48, FDR-adjusted p = 0.056), which was marginally significant (Fig. 5).

Finally, in the WM, a strong positive correlation was found between R1 and the intensity fraction and the diffusivity of the intra-neurite compartment (namely, fneurite and D_{in}). After controlling for the confounding effect of ROI volume, only the association between D_{in} and R1 remained significant (Table 2). These results reinforce the notion that the intra-neurite diffusivity serves as a reliable proxy for myelin content in WM. The observed associations highlight how diffusion-weighted imaging has the potential to capture changes in microstructural integrity related to myelination, which is crucial for understanding both neurodevelopmental processes and age-related changes in brain structure (Salat et al., 2005; Song et al., 2002). The strong positive correlations found in WM suggest that as myelin content increases, so do the intra-neurite characteristics reflected by D_{in}. This relationship is critical for elucidating how WM integrity supports efficient neural communication across different brain regions.

4.3. Limitations and implications for future research

One of the primary limitations of this study stems from the physical and technical constraints of the 3 T scanner used, which has a maximum gradient strength of 80 mT/m. Achieving a maximum b-value of 6000 s/mm^2 required a gradient pulse duration (δ) of 28 ms and a time between pulses (Δ) of 40 ms, resulting in an effective diffusion time ($\Delta - \delta/3$) of approximately 31 ms. This diffusion time is around 50 % longer than the 20 ms recommended in previous studies (Jelescu et al., 2022; Olesen

et al., 2022; Palombo et al., 2020), where a non-exchanging multi--compartment model can be used with minimal bias due to unaccounted exchange mechanisms. The use of longer gradient pulses (28 ms) and diffusion times (31 ms) in this study could result in unaccounted exchange between neurites and the extracellular compartment (occurring in the order of 20–50 ms in vivo, according to animal studies by (Jelescu et al., 2022)). Using the Neurite Exchange Imaging (NEXI) model to simulate the impact of such exchange, we estimated that the unaccounted exchange between diffusion compartments in SANDI could lead to a potential underestimation of fneurite by up to 8 % and D_e by up to 16 %, and an overestimation of Rsoma by up to 4 %. However, while these exchange effects cannot be disregarded at the diffusion time employed, their contribution to bias in parameter estimates is likely lower than or comparable to the noise-related bias for SNR∼100, which is the case of this study (Schiavi et al., 2023).

Secondly, the fitting approach to derive the diffusion-metrics via SANDI model (linear and regularized fitting versus machine learning non-linear fitting, for instance) can lead to slightly different parameter estimates. To improve comparability and harmonization across studies, future research should adopt consistent fitting strategies. Additionally, refining noise and distortion correction algorithms in the DWI preprocessing phase and comparing different machine learning algorithms for diffusion-metrics estimation could further improve the robustness of the obtained findings.

A third limitation of the present study is represented by the premises of the MP2RAGE technique to map R1, i.e., the assumption that each voxel comprises a single spin pool of water molecules, whose signal recovery after excitation can be theoretically described by a mono-exponential behavior. This model faces limitations due to factors like the complexity of tissue composition and the influence of magnetization transfer effects (van Gelderen et al., 2016). Indeed, myelin has a complex structure with bound water molecules and different T1 relaxation properties than free water. Moreover, T1 relaxation in WM is not solely determined by myelin. Factors like tissue iron content (Gelman et al., 2001), water-to-macromolecule ratio, i.e. effectively the water content, axonal density, and the size of axons (Harkins et al., 2016) can also influence T1. Besides that, we acknowledge that mono-exponential fits of longitudinal relaxation may oversimplify the inherently multi-exponential nature of the GM, characterized by a complex cytoarchitecture with a higher density of cell bodies, dendrites and synapses (Jamarik et al., 2022).

As pertains to WM, other approaches exist to estimate both the short and long longitudinal relaxation components, such as inversion recovery fast-spin echo (IR-FSE) with multiple inversion times, or an MP2RAGE pulse sequence opportunely tuned, as shown in Rioux et al. (Rioux et al., 2016). In this work the authors estimated the expected bias in measuring the long T1 component as a function of the chosen TIs. This bias could not be determined in our case, as only the first TI was in the range tested by the authors. Future work will focus on exploring the biexponential relaxation in both WM and GM using clinically viable sequences such as MP2RAGE.

For the present study, which examined correlations between MP2RAGE-derived 'apparent' R1 and SANDI-derived metrics, assuming that inaccurate modeling introduced a systematic bias of the quantified R1 per tissue type (Saunders et al., 2025), correlations are expected to be preserved. Besides that, the role of confounding factors such as water and iron content, contributing to R1 contrast can be determined by using additional protocols. Future studies would ideally combine T1 mapping with complementary indices such as proton density or quantitative magnetization transfer, which better disentangle water content and macromolecular contributions.

Finally, by performing a post hoc power analysis on our data, the achieved power in detecting significant correlations between SANDI metrics and R1, given our sample size of $N = 20$ (assuming a single tail test and a coefficient of determination R^2=0.25, taking into account the correlation between fsoma and R1) is 76 %. Based on this analysis, our study is slightly underpowered, bringing a slightly higher risk of missing true effects (or finding significant correlations between SANDI metrics and R1).

Despite these limitations, our results highlight a significant association between cortical R1 and diffusion-derived microstructural metrics, highlighting the utility of combining R1 mapping with SANDI-based diffusion modeling and underlining the contribution of GM cytoarchitecture into R1 contrast. Future research should explore whether these relationships hold in clinical populations, particularly in conditions characterized by demyelination or altered cortical microstructure, such as Multiple Sclerosis or other neurodegenerative disorders (Schmierer et al., 2008; Shafee et al., 2015). Investigating longitudinal changes in R1 and SANDI-derived metrics could provide valuable insights into disease progression and treatment response, proving useful also for advancing research in personalized medicine. Another important direction for future studies should focus on the relationship between learning-induced microstructural changes, as reflected by SANDI metrics and R1. Such research could provide further insights into the processes driving brain adaptability and resilience, shedding light on the dynamic nature of structural and functional plasticity in the human brain.

5. Conclusions

We found that microstructural metrics derived from the SANDI model fitting of diffusion-weighted data are significantly associated with R1 estimated via MP2RAGE. The observed correlations support the role of GM cytoarchitecture in shaping R1 contrast in GM and highlight the potential of SANDI to probe cortical microstructure related to myelination. Moreover, the findings highlighted the structural diversity of cortical GM, potentially linked to its role in supporting neuroplasticity and complex cognitive functions. The correlations found in WM validated the utility of diffusion metrics as reliable biomarkers for assessing myelin integrity in WM.

Continued methodological advancements are necessary to refine diffusion-based metrics and expand their applicability in both research and clinical settings, and to make advantage of clinically viable methods optimized to be sensitive to different relaxation components. By addressing current limitations and integrating multi-parametric and multimodal imaging approaches, future studies will contribute to a deeper understanding of the structural and functional architecture of the brain in both health and disease.

Data availability

The data that supports the findings of this study are available from the corresponding author, upon reasonable request. The code used for correlation analysis is available at (https://github.com/caporaleas/STR_CORR) and for diffusion data quality check at (https://github.com/caporaleas/STR_DWI).

CRediT authorship contribution statement

E. Bliakharskaia: Writing – original draft, Formal analysis. **A.M. Chiarelli:** Writing – review & editing, Supervision, Project administration, Funding acquisition. **E. Patitucci:** Writing – review & editing, Investigation, Data curation. **M. Carriero:** Software, Formal analysis. **D. Di Censo:** Software, Formal analysis. **E. Biondetti:** Writing – review & editing, Visualization. **C. Del Gratta:** Writing – review & editing, Supervision. **S. Capuani:** Writing – review & editing, Visualization. **M. Palombo:** Writing – review & editing, Methodology. **V. Tomassini:** Writing – review & editing. **R.G. Wise:** Writing – review & editing, Supervision, Project administration, Funding acquisition. **A. Caporale:** Writing – review & editing, Writing – original draft, Visualization, Supervision, Software, Methodology, Formal analysis, Conceptualization.

Declaration of competing interest

The authors confirm that this research was performed without any commercial or financial interests that could be perceived as a potential conflict of interest.

Acknowledgements

European Union-Next Generation EU- Italian Ministry of University and Research (MUR), Research National Program (PNR) and Projects of National Relevance (PRIN), Project Code: 2022BERM2F, Project Title: "Mapping Mitochondrial Function and Oxygen Metabolism in the Human Brain with Magnetic Resonance Imaging." Funding call No 104 of 02.02.2022, Concession decree No 1065 of 18.07.2023 adopted by MUR, ERC Panel LS7 "Prevention, Diagnosis and Treatment of Human Diseases". CUP: D53D23013410001;

European Union-NextGenerationEU- Italian Ministry of University and Research (MUR), National Plan for Recovery and Resilience (PNRR) and Projects of National Relevance (PRIN), Project Code: P20225AEEE, Project Title: "Hybrid PET-MRI to simultaneously probe brain metabolism and cerebrovascular function in neurodegenerative diseases." Funding call No 1409 of 14.09.2022, Concession decree No 1369 of 01.09.2023 adopted by MUR, ERC Panel LS7 "Prevention, Diagnosis and Treatment of Human Diseases". CUP: D53D23021480001;

European Union-NextGenerationEU- Italian Ministry of University and Research (MUR), National Plan for Recovery and Resilience (PNRR) and Projects of National Relevance (PRIN), Project Code: P2022ESHT4, Project Title: "Advancing MRI biomarkers of brain tissue microstructure and energetics in Multiple Sclerosis." Funding call No 1409 of 14.09.2022, Concession decree No 1367 of 01.09.2023 adopted by MUR, ERC Panel LS5"Neuroscience and Disorders of the Nervous System". CUP: D53D23019210001;

European Union - NextGenerationEU under the National Plan for Recovery and Resilience (PNRR), Mission 4 Component 2 - M4C2, Investment 1.5 - Call for tender No 3277 of 30.12.2021 Italian Ministry of Universities Award Number: ECS00000041, Project Title: "VITALITY - Innovation, digitalization and sustainability for the diffused economy in Central Italy," Concession Decree No 1057 of 23.06.2022 adopted by the Italian Ministry of University and Research. CUP D73C22000840006;

European Union - Next Generation EU under the National Plan for Recovery and Resilience (PNRR), Project Title: "MNESYS (PE0000006) - A Multiscale integrated approach to the study of the nervous system in health and disease," Concession Decree No 1553 of 11.10.2022 adopted by the Italian Ministry of University and Research;

EB has received funding from the European Union's Horizon Europe research and innovation programme under the Marie Skłodowska-Curie Grant Agreement No 101066055-acronym HERMES. Views and opinions expressed are however those of the author(s) only and do not necessarily reflect those of the European Union or the European Research Executive Agency (REA). Neither the European Union nor the granting authority can be held responsible for them. MP is supported by the UKRI Future Leaders Fellowship (MR/T020296/2);

AC is partially supported by the Fund for the Promotion and Development of Policies of the National Research Program - as per DM 737/2021 issued by the MUR;

EB is supported by Doctorate School of the Gabriele D'Annunzio University;

MP is funded by the UKRI Future Leaders Fellowship MR/T020296/2;

EP was supported by Wellcome Trust Ph.D. studentship [203965/Z/16/Z] and partially supported by the UK Engineering and Physical Sciences Research Council (EP/S025901/1).

Supplementary materials

Supplementary material associated with this article can be found, in the online version, at doi:10.1016/j.neuroimage.2025.121466.

Data availability

Data will be made available on request.

References

Afzali, M., Nilsson, M., Palombo, M., Jones, D.K., 2021. SPHERIOUSLY? The challenges of estimating sphere radius non-invasively in the human brain from diffusion MRI. Neuroimage 237, 118183. https://doi.org/10.1016/j.neuroimage.2021.118183.

Alexander, D.C., Dyrby, T.B., Nilsson, M., Zhang, H., 2019. Imaging brain microstructure with diffusion MRI: practicality and applications. NMR Biomed. 32, e3841. https://doi.org/10.1002/nbm.3841.

Berg, R.C., Leutritz, T., Weiskopf, N., Preibisch, C., 2022. Multi-parameter quantitative mapping of R1, R2*, PD, and MTsat is reproducible when accelerated with Compressed SENSE. Neuroimage 253, 119092. https://doi.org/10.1016/j.neuroimage.2022.119092.

Call, C.L., Bergles, D.E., 2021. Cortical neurons exhibit diverse myelination patterns that scale between mouse brain regions and regenerate after demyelination. Nat. Commun. 12, 4767. https://doi.org/10.1038/s41467-021-25035-2.

Callaghan, M.F., Helms, G., Lutti, A., Mohammadi, S., Weiskopf, N., 2015. A General Linear Relaxometry Model of R1 Using Imaging Data. Magn. Reson. Med. 73, 1309–1314. https://doi.org/10.1002/mrm.25210.

Caporale, A., Palombo, M., Macaluso, E., Guerreri, M., Bozzali, M., Capuani, S., 2017. The γ-parameter of anomalous diffusion quantified in human brain by MRI depends on local magnetic susceptibility differences. Neuroimage 147, 619–631. https://doi.org/10.1016/j.neuroimage.2016.12.051.

Davies, G.R., Ramió-Torrentà, L., Hadjiprocopis, A., Chard, D.T., Griffin, C.M.B., Rashid, W., Barker, G.J., Kapoor, R., Thompson, A.J., Miller, D.H., 2004. Evidence for grey matter MTR abnormality in minimally disabled patients with early relapsing-remitting multiple sclerosis. Journal of Neurology, Neurosurgery & Psychiatry 75, 998–1002. https://doi.org/10.1136/jnnp.2003.021915.

Desmond, K.L., Al-Ebraheem, A., Janik, R., Oakden, W., Kwiecien, J.M., Dabrowski, W., Rola, R., Geraki, K., Farquharson, M.J., Stanisz, G.J., Bock, N.A., 2016. Differences in iron and manganese concentration may confound the measurement of myelin from R1 and R2 relaxation rates in studies of dysmyelination. NMR Biomed. 29, 985–998. https://doi.org/10.1002/nbm.3549.

Dicke, U., Roth, G., 2016. Neuronal factors determining high intelligence. Philos. Trans. R. Soc. Lond. B Biol. Sci. 371, 20150180. https://doi.org/10.1098/rstb.2015.0180.

Dietrich, O., Raya, J.G., Reeder, S.B., Reiser, M.F., Schoenberg, S.O., 2007. Measurement of signal-to-noise ratios in MR images: influence of multichannel coils, parallel imaging, and reconstruction filters. J. Magn. Reson. Imaging 26, 375–385. https://doi.org/10.1002/jmri.20969.

Eickhoff, S., Walters, N.B., Schleicher, A., Kril, J., Egan, G.F., Zilles, K., Watson, J.D.G., Amunts, K., 2005. High-resolution MRI reflects myeloarchitecture and cytoarchitecture of human cerebral cortex. Hum. Brain Mapp. 24, 206–215. https://doi.org/10.1002/hbm.20082.

Fischl, B., 2012. FreeSurfer. NeuroImage, 20 YEARS OF fMRI 62, 774–781. https://doi.org/10.1016/j.neuroimage.2012.01.021.

Gelman, N., Ewing, J.R., Gorell, J.M., Spickler, E.M., Solomon, E.G., 2001. Interregional variation of longitudinal relaxation rates in human brain at 3.0 T: relation to estimated iron and water contents. Magn. Reson. Med. 45, 71–79. https://doi.org/10.1002/1522-2594(200101)45:1<71::aid-mrm1011>3.0.co;2-2.

Glasser, M.F., Coalson, T.S., Robinson, E.C., Hacker, C.D., Harwell, J., Yacoub, E., Ugurbil, K., Andersson, J., Beckmann, C.F., Jenkinson, M., Smith, S.M., Van Essen, D. C., 2016. A multi-modal parcellation of human cerebral cortex. Nature 536, 171–178. https://doi.org/10.1038/nature18933.

Glasser, M.F., Goyal, M.S., Preuss, T.M., Raichle, M.E., Van Essen, D.C., 2014. Trends and properties of human cerebral cortex: correlations with cortical myelin content. Neuroimage 93 (Pt 2), 165–175. https://doi.org/10.1016/j.neuroimage.2013.03.060.

Guerreri, M., Palombo, M., Caporale, A., Fasano, F., Macaluso, E., Bozzali, M., Capuani, S., 2019. Age-related microstructural and physiological changes in normal brain measured by MRI γ-metrics derived from anomalous diffusion signal representation. Neuroimage 188, 654–667. https://doi.org/10.1016/j.neuroimage.2018.12.044.

Harkins, K.D., Xu, J., Dula, A.N., Li, K., Valentine, W.M., Gochberg, D.F., Gore, J.C., Does, M.D., 2016. The microstructural correlates of T1 in white matter. Magn. Reson. Med. 75, 1341–1345. https://doi.org/10.1002/mrm.25709.

Hutter, J., Tournier, J.D., Price, A.N., Cordero-Grande, L., Hughes, E.J., Malik, S., Steinweg, J., Bastiani, M., Sotiropoulos, S.N., Jbabdi, S., Andersson, J., Edwards, A. D., Hajnal, J.V., 2018. Time-efficient and flexible design of optimized multishell HARDI diffusion. Magn. Reson. Med. 79, 1276–1292. https://doi.org/10.1002/mrm.26765.

Jamarik, J., Vojtišek, L., Schwarz, D., 2022. Uncovering cortical layers with multi-exponential analysis: a region of interest study. In: 2022 30th European Signal Processing Conference (EUSIPCO). Presented at the 2022 30th European Signal Processing Conference (EUSIPCO), pp. 1353–1356. https://doi.org/10.23919/EUSIPCO55093.2022.9909806.

Jelescu, I.O., de Skowronski, A., Geffroy, F., Palombo, M., Novikov, D.S., 2022. Neurite Exchange Imaging (NEXI): a minimal model of diffusion in gray matter with inter-compartment water exchange. Neuroimage 256, 119277. https://doi.org/10.1016/j.neuroimage.2022.119277.

Jenkinson, M., Beckmann, C.F., Behrens, T.E.J., Woolrich, M.W., Smith, S.M., 2012. FSL. Neuroimage 62, 782–790. https://doi.org/10.1016/j.neuroimage.2011.09.015.
Jones, D.K., 2010. Diffusion MRI. Oxford University Press.
Jones, D.K., Basser, P.J., 2004. Squashing peanuts and smashing pumpkins": how noise distorts diffusion-weighted MR data. Magn. Reson. Med. 52, 979–993. https://doi.org/10.1002/mrm.20283.
Jones, D.K., Knösche, T.R., Turner, R., 2013. White matter integrity, fiber count, and other fallacies: the do's and don'ts of diffusion MRI. Neuroimage 73, 239–254. https://doi.org/10.1016/j.neuroimage.2012.06.081.
Krijnen, E.A., Russo, A.W., Salim Karam, E., Lee, H., Chiang, F.L., Schoonheim, M.M., Huang, S.Y., Klawiter, E.C., 2023. Detection of grey matter microstructural substrates of neurodegeneration in multiple sclerosis. Brain Commun. 5, fcad153. https://doi.org/10.1093/braincomms/fcad153.
Kutzelnigg, A., Lucchinetti, C.F., Stadelmann, C., Brück, W., Rauschka, H., Bergmann, M., Schmidbauer, M., Parisi, J.E., Lassmann, H., 2005. Cortical demyelination and diffuse white matter injury in multiple sclerosis. Brain 128, 2705–2712. https://doi.org/10.1093/brain/awh641.
Lutti, A., Dick, F., Sereno, M.I., Weiskopf, N., 2014. Using high-resolution quantitative mapping of R1 as an index of cortical myelination. Neuroimage 93, 176–188. https://doi.org/10.1016/j.neuroimage.2013.06.005.
Marques, J.P., Kober, T., Krueger, G., Van Der Zwaag, W., Van De Moortele, P.-F., Gruetter, R., 2010. MP2RAGE, a self bias-field corrected sequence for improved segmentation and T1-mapping at high field. Neuroimage 49, 1271–1281. https://doi.org/10.1016/j.neuroimage.2009.10.002.
McKinnon, E.T., Jensen, J.H., Glenn, G.R., Helpern, J.A., 2017. Dependence on b-value of the direction-averaged diffusion-weighted imaging signal in brain. Magn. Reson. ImAging 36, 121–127. https://doi.org/10.1016/j.mri.2016.10.026.
Mori, S., Oishi, K., Jiang, H., Jiang, L., Li, X., Akhter, K., Hua, K., Faria, A.V., Mahmood, A., Woods, R., Toga, A.W., Pike, G.B., Neto, P.R., Evans, A., Zhang, J., Huang, H., Miller, M.I., van Zijl, P., Mazziotta, J., 2008. Stereotaxic white matter atlas based on diffusion tensor imaging in an ICBM template. Neuroimage 40, 570–582. https://doi.org/10.1016/j.neuroimage.2007.12.035.
Mottershead, J.P., Schmierer, K., Clemence, M., Thornton, J.S., Scaravilli, F., Barker, G. J., Tofts, P.S., Newcombe, J., Cuzner, M.L., Ordidge, R.J., McDonald, W.I., Miller, D. H., 2003. High field MRI correlates of myelin content and axonal density in multiple sclerosis–a post-mortem study of the spinal cord. J. Neurol. 250, 1293–1301. https://doi.org/10.1007/s00415-003-0192-3.
Mukherjee, P., Miller, J.H., Shimony, J.S., Philip, J.V., Nehra, D., Snyder, A.Z., Conturo, T.E., Neil, J.J., McKinstry, R.C., 2002. Diffusion-Tensor MR Imaging of Gray and White Matter Development during Normal Human Brain Maturation. American Journal of Neuroradiology 23, 1445–1456.
Novikov, D.S., Fieremans, E., Jensen, J.H., Helpern, J.A., 2011. Random walks with barriers. Nature Phys 7, 508–514. https://doi.org/10.1038/nphys1936.
Novikov, D.S., Jensen, J.H., Helpern, J.A., Fieremans, E., 2014. Revealing mesoscopic structural universality with diffusion. Proceedings of the National Academy of Sciences 111, 5088–5093. https://doi.org/10.1073/pnas.1316944111.
Olesen, J.L., Østergaard, L., Shemesh, N., Jespersen, S.N., 2022. Diffusion time dependence, power-law scaling, and exchange in gray matter. Neuroimage 251, 118976. https://doi.org/10.1016/j.neuroimage.2022.118976.
Palombo, M., Ianus, A., Guerreri, M., Nunes, D., Alexander, D.C., Shemesh, N., Zhang, H., 2020. SANDI: a compartment-based model for non-invasive apparent soma and neurite imaging by diffusion MRI. Neuroimage 215, 116835. https://doi.org/10.1016/j.neuroimage.2020.116835.
Palombo, M., Shemesh, N., Ianus, A., Alexander, D., Zhang, H., 2018. Abundance of cell bodies can explain the stick model's failure in grey matter at high bvalue. In: Presented at the Joint Annual Meeting ISMRM-ESMRMB 2018.
Rioux, J.A., Levesque, I.R., Rutt, B.K., 2016. Biexponential longitudinal relaxation in white matter: characterization and impact on T1 mapping with IR-FSE and MP2RAGE. Magn. Reson. Med. 75, 2265–2277. https://doi.org/10.1002/mrm.25729.
Salat, D.H., Tuch, D.S., Greve, D.N., van der Kouwe, A.J.W., Hevelone, N.D., Zaleta, A.K., Rosen, B.R., Fischl, B., Corkin, S., Rosas, H.D., Dale, A.M., 2005. Age-related alterations in white matter microstructure measured by diffusion tensor imaging. Neurobiol. Aging 26, 1215–1227. https://doi.org/10.1016/j.neurobiolaging.2004.09.017.
Saunders, A.M., Kim, M.E., Gao, C., Remedios, L.W., Krishnan, A.R., Schilling, K.G., O'Grady, K.P., Smith, S.A., Landman, B.A., 2025. Comparison and calibration of MP2RAGE quantitative T1 values to multi-TI inversion recovery T1 values. Magn. Reson. ImAging 117, 110322. https://doi.org/10.1016/j.mri.2025.110322.
Schiavi, S., Palombo, M., Zacà, D., Tazza, F., Lapucci, C., Castellan, L., Costagli, M., Inglese, M., 2023. Mapping tissue microstructure across the human brain on a clinical scanner with soma and neurite density image metrics. Hum. Brain Mapp. 44, 4792–4811. https://doi.org/10.1002/hbm.26416.
Schmierer, K., Scaravilli, F., Altmann, D.R., Barker, G.J., Miller, D.H., 2004. Magnetization transfer ratio and myelin in postmortem multiple sclerosis brain. Ann. Neurol. 56, 407–415. https://doi.org/10.1002/ana.20202.
Schmierer, K., Wheeler-Kingshott, C.A.M., Tozer, D.J., Boulby, P.A., Parkes, H.G., Yousry, T.A., Scaravilli, F., Barker, G.J., Tofts, P.S., Miller, D.H., 2008. Quantitative magnetic resonance of postmortem multiple sclerosis brain before and after fixation. Magn. Reson. Med. 59, 268–277. https://doi.org/10.1002/mrm.21487.
Shafee, R., Buckner, R.L., Fischl, B., 2015. Gray matter myelination of 1555 human brains using partial volume corrected MRI images. Neuroimage 105, 473–485. https://doi.org/10.1016/j.neuroimage.2014.10.054.
Song, S.-K., Sun, S.-W., Ramsbottom, M.J., Chang, C., Russell, J., Cross, A.H., 2002. Dysmyelination revealed through MRI as increased radial (but unchanged axial) diffusion of water. Neuroimage 17, 1429–1436. https://doi.org/10.1006/nimg.2002.1267.
Sullivan, E.V., Pfefferbaum, A., 2010. Diffusion Tensor Imaging in Aging and Age-Related Neurodegenerative Disorders. In: Jones, P., Derek, K. (Eds.), Diffusion MRI: Theory, Methods, and Applications. Oxford University Press, p. 0. https://doi.org/10.1093/med/9780195369779.003.0038.
Tournier, J.-D., Smith, R., Raffelt, D., Tabbara, R., Dhollander, T., Pietsch, M., Christiaens, D., Jeurissen, B., Yeh, C.-H., Connelly, A., 2019. MRtrix3: a fast, flexible and open software framework for medical image processing and visualisation. Neuroimage 202, 116137. https://doi.org/10.1016/j.neuroimage.2019.116137.
Turner, R., 2019. Myelin and Modeling: bootstrapping Cortical Microcircuits. Front. Neural Circuits. 13, 34. https://doi.org/10.3389/fncir.2019.00034.
van Gelderen, P., Jiang, X., Duyn, J.H., 2016. Effects of Magnetization Transfer on T1 Contrast in Human Brain White Matter. Neuroimage 128, 85–95. https://doi.org/10.1016/j.neuroimage.2015.12.032.
Veraart, J., Novikov, D.S., Christiaens, D., Ades-aron, B., Sijbers, J., Fieremans, E., 2016. Denoising of diffusion MRI using random matrix theory. Neuroimage 142, 394–406. https://doi.org/10.1016/j.neuroimage.2016.08.016.
Walters, N.B., Egan, G.F., Kril, J.J., Kean, M., Waley, P., Jenkinson, M., Watson, J.D.G., 2003. In vivo identification of human cortical areas using high-resolution MRI: an approach to cerebral structure–function correlation. Proc. Natl. Acad. Sci. U.S.A. 100, 2981–2986. https://doi.org/10.1073/pnas.0437896100.
Weiskopf, N., Suckling, J., Williams, G., Correia, M.M., Inkster, B., Tait, R., Ooi, C., Bullmore, E.T., Lutti, A., 2013. Quantitative multi-parameter mapping of R1, PD*, MT, and R2* at 3T: a multi-center validation. Front. Neurosci. 7. https://doi.org/10.3389/fnins.2013.00095.
Yang, D.M., Huettner, J.E., Bretthorst, G.L., Neil, J.J., Garbow, J.R., Ackerman, J.J.H., 2018. Intracellular water preexchange lifetime in neurons and astrocytes. Magnetic Resonance in Med 79, 1616–1627. https://doi.org/10.1002/mrm.26781.